

Research Article

Effect of Brittle Mineral Size on Hydraulic Fracture Propagation in Shale Gas Reservoir

Wei Gao ¹, Javed Iqbal ^{2,3}, Dan Xu ⁴, Haoyue Sui ^{1,5} and Ruilin Hu ¹

¹Key Laboratory of Shale Gas and Geoenvironment, Institute of Geology and Geophysics, Chinese Academy of Sciences, No. 19, Beitucheng Western Road, Chaoyang District, Beijing 100029, China

²Department of Earth Sciences, Abbottabad University of Science and Technology, Pakistan

³Key Laboratory for Mountain Hazards and Earth Surface Process, Institute of Mountain Hazards & Environment, Chinese Academy of Sciences, Chengdu, China

⁴China Railway 11th Bureau Group Co. Ltd., No. 277, Zhongshan Road, Wuchang District, Wuhan, Hubei Province, China

⁵University of Chinese Academy of Sciences, Beijing 100049, China

Correspondence should be addressed to Wei Gao; gaowei@mail.iggcas.ac.cn and Javed Iqbal; javediqbalgeo@gmail.com

Received 18 July 2018; Revised 1 October 2018; Accepted 9 October 2018; Published 30 January 2019

Academic Editor: Baojun Bai

Copyright © 2019 Wei Gao et al. This is an open access article distributed under the Creative Commons Attribution License, which permits unrestricted use, distribution, and reproduction in any medium, provided the original work is properly cited.

The properties of brittle minerals have great effect on the morphology of postfracturing network in shale reservoirs in the southeastern Ordos Basin, China. In order to study the effect of brittle mineral size distributions on the fracture parameters, the concrete cubes of 300 mm × 300 mm × 300 mm in size with four distinct brittle mineral sizes of 2.36 mm, 0.425 mm, 0.15 mm, and 0.075 mm were investigated under large-sized triaxial hydraulic fracturing test. The effect mechanism of aggregate on the fracture properties of shale was studied using ultrasonic technique, photosensitive electron microscope, and numerical simulation. The test results obtained for each specimen (both disturbed and undisturbed conditions) indicate that brittle mineral size has significant effect on the fracture extension. The tensile strength, fracture toughness, and fracture pressure were found to decrease with a decrease in maximum brittle mineral size when the maximum brittle mineral size is smaller than 0.425 mm. In addition to this, the degree of attenuation difference also follows the similar trend. Observed fracture morphology reveals that with an increase in maximum size of brittle mineral specimen, the tortuous and complicated cracking path generation increases. These findings would be very helpful in order to better understand the behavior of shale under hydraulic fracturing test.

1. Introduction

Shale is a fine-grained sedimentary rock composed primarily of clay, organics, and brittle minerals such as quartz, feldspar, and pyrite. It is the most common sedimentary rock and is of particular interest with respect to shale gas production in China [1–7]. Heterogeneously resulted from pores, preexisting cracks and brittle mineral that exist in the shale may impact the mechanical properties and the fracture pattern of the formation which can potentially affect the performance of hydraulic fracturing operations and the production rate [8–10]. During hydraulic fracturing, shales with a high percentage of brittle minerals such as quartz and carbonate as well as the presence of feldspar provide more easy fracturing and breaking to a tree-shaped network fractures, which

provide numerous flow paths from the reservoir to the wellbore [11, 12]. On the contrary, the high amount of ductile clays results in the deformation of tabular fractures, which are not favorable for shale stimulation operation [13].

The shale gas fields which are under development possess well-developed natural fracture systems normally due to very high brittle mineral content which increases the brittleness of the shale. In the Ohio, Woodford, and Barnett shales, the contents of quartz, feldspar, and pyrite are 20%–80% (Figure 1(a)) [14–16]. In the Barnett Formation of Mississippi system in the Fort Worth Basin, gas-producing dark calcic-siliceous shale has a quartz content of 35%–50%, with an average of about 45% [17, 18]. In North America, the Devonian and Carboniferous shale gas reservoirs have high content of quartz, mostly >40%, some up to 75% [19]. In

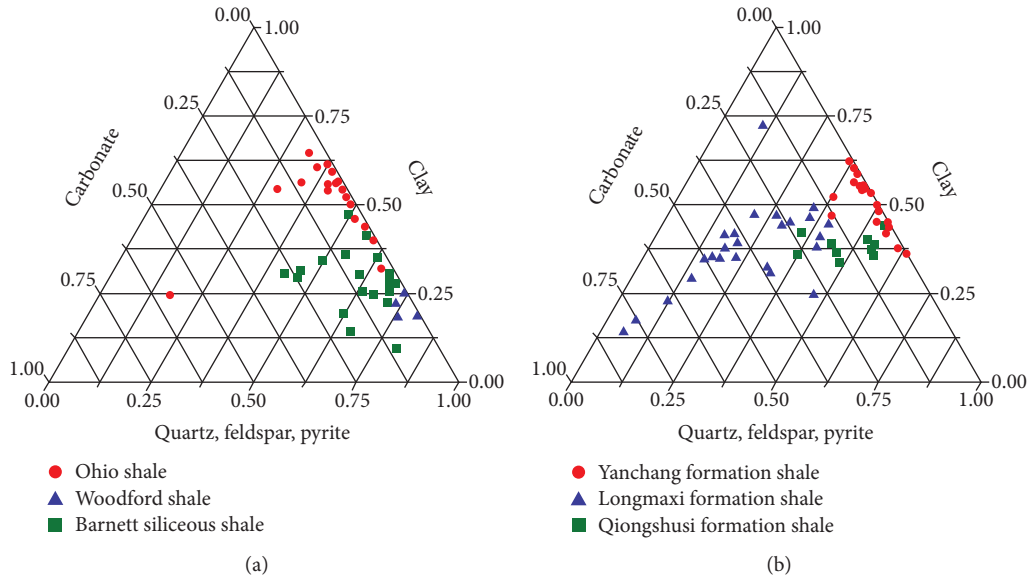


FIGURE 1: Ternary diagrams showing mineral compositions of shale reservoirs.

the Sichuan Basin in China (Figure 1(b)), the Lower Cambrian Qiongzhusi dark shale reservoirs have the quartz content ranging from 46.5% to 69.2% (av. 57.5%). In the Lower Silurian Longmaxi Formation, the shale is rich in plagioclase and has high quartz content ranging from 34.7% and 83.4% (avg. 55.1%) [20]. The average quartz content of shale gas formations in the Yanchang Formation in Ordos Basin is 20–64%, with a carbonate content of 1–14%, and the total brittle mineral content on average is 58.2% [21]. In brittle minerals, silica content is generally higher than 40%, and clay mineral content is less than 30% for shale that can be commercially exploited [13].

As a key factor affecting the morphology of postfracturing network in the shale reservoir, the properties of its basic constituents, specifically the characteristics of brittle minerals, have always been a matter of discussion in the research community. Brittleness indices based on rock composition and the fraction of brittle mineral content were proposed by many researchers [22–25].

However, the developmental degrees of natural and induced fractures not only depend on brittle mineral content but also have a relationship with brittle mineral size. Recent studies showed that strong heterogeneity of the lithology exists within the Upper Triassic continental shales in the southeastern Ordos Basin in China, especially the different sizes of detrital grains which combine mud matrix or organic matter [26]. Various lithological combination patterns may lead to dissimilarity in rock mechanics which has great impact on the response of shale to hydraulic fracturing [27]. Hence, in-depth study is required to analyze how brittle mineral size controls the shale fracture development.

In this paper, the possible impact of brittle minerals during the hydraulic fracture process of specimens is discussed. A series of experiments using a large-sized triaxial hydraulic fracturing system were conducted on the influence of brittle mineral size and fracture toughness of specimens. Ultrasonic technique, photosensitive electron microscope,

and numerical simulation were used to detect the fracture process in a real-time setting.

2. Experimental Details

2.1. Sample Preparation. In the Chang-7 (C7) member, the Yanchang Formation in the southeastern Ordos Basin, 31%–78% of brittle minerals (avg. 42.3%) were found in a shale from Well Yaoke-1. Among the brittle minerals, quartz and feldspar were dominated. Thin-section investigation of shale samples in the C7 member shows that different sizes of brittle minerals from 0.03 mm to 2 mm exist within the continental shales (Figure 2). In order to get the better results and suitability of sample preparation, we prepared artificial concrete samples using the lithological characteristics of Well Yaoke-1.

GB175-2007 type P.O32.5 was prepared by the Yanxin Cement Factory in Hubei Province, with a 28-day compressive strength of 32.5 MPa. The clay mineral used was illite powder and had specific surface of 60 m²/g. The brittle material used was fine silica sand (quarried in Ling Shou County, Hebei Province) with maximum sizes of 2.36, 0.425, 0.15, and 0.075 mm, respectively (Figure 3). It was noticed that the particles of each silica sand sample had uniform angularity characteristics. The bulk specific gravity is 2.65, and all of the silica sand was provided by one factory.

Water, sand, clay powder, and cement were mixed for 10 minutes to ensure that the sand grain distribution remains the uniform in the mortar. The mix was poured gradually into a metal mold with an inner space of 300 mm³ while a vibration table was used to remove the air bubbles trapped in the mix. The vibration time period was chosen in such a way that sand particles were not settling as mixture viscosity but were relatively large to suspend them during the course of vibration. The mix proportions of the samples are given in Table 1.

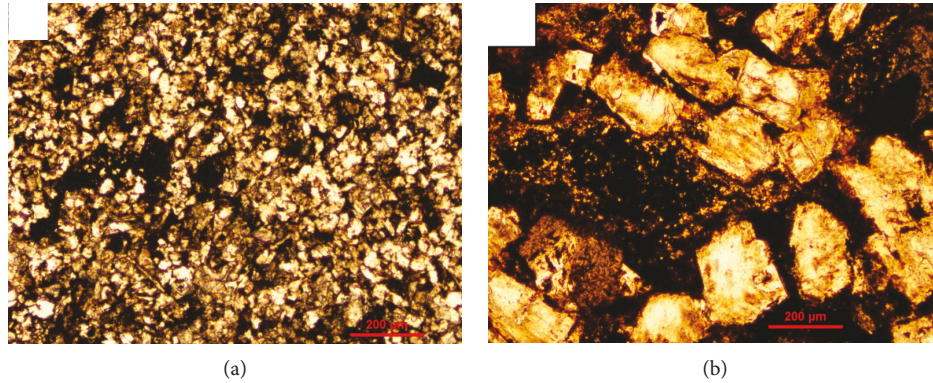


FIGURE 2: The thin sections of shale samples in the C7 member: (a) shale with small brittle mineral; (b) shale with large brittle mineral.



FIGURE 3: Different particle sizes of silica sand: (a) maximum size of 2.36 mm; (b) maximum size of 0.425 mm; (c) maximum size of 0.15 mm; (d) maximum size of 0.075 mm.

After vibration, perforated casing was placed at the center of the mold with a buried depth of 20 cm and perforation length of 10 cm and spirally distributed perforation holes with 1 cm height difference and 90 degrees of angular difference between the adjacent holes. In order to keep the perforation holes open, small adhesive tapes were used to paste each of the perforation holes. Figure 4 shows the schematic and actual diagrams of the prepared hydrofracturing specimen. Samples were removed carefully from the mold after 12 hours and cured for 28 days in 20°C water bath.

2.2. Experimental Design. In order to investigate the function of brittle materials during hydraulic fracture process of shale, the hydraulic fracture experiments were carried out and the fracture parameters of samples with different brittle mineral sizes were studied before and after experiments by ultrasonic technique.

2.2.1. Rock Mechanic Tests. Before hydraulic fracturing experiments, some of these blocks were used as samples and the rock mechanic tests were performed to estimate the

tensile strength (σ_t) and fracture toughness (K_{IC}) of the samples with different brittle material sizes; Brazilian tests and cracked chevron-notched Brazilian disc (CCNBD) tests were conducted on 27 cylindrical samples with sizes of 50 mm × 26 mm in (diameter × thickness) for tensile strength and 18 cylindrical samples with sizes of 75 mm × 30 mm in (diameter × thickness) for fracture toughness, respectively, according to the ISRM recommendation for concrete. The average fracture toughness K_{IC} and tensile strength with different brittle material sizes are given in Table 1.

2.2.2. Hydraulic Fracture Experiments. Hydraulic fracturing tests were performed in a triaxial pressure machine using the relevant methods given by Ishida et al. [28, 29]. A diagram of the system used for the fracturing experiment is shown in Figure 5. Laboratory equipment used for the experiments includes a triaxial loading system using hydraulic jacks, a servo hydraulic pump, a servo control cabinet, and a data acquisition system. Cubic samples with each side of 300 mm were placed between the pressurized pistons for simulating in situ stress conditions. A flat steel plate covered on both sides with Vaseline was inserted between the model block and the pressure plate to avoid shear stress.

The stresses were applied to the sample along the principal stress directions, i.e., the maximum horizontal geostress (σ_H), the minimum horizontal geostress (σ_h), and the vertical stress (σ_V). The horizontal stress difference, K_h , is one of the important factors affecting the hydraulic fracture extension. In order to make the test stress setting more reliable, the vertical stress σ_V was set at 2.25 MPa, the minimum horizontal principal stress σ_h was set at 0.9 MPa, and the maximum horizontal principal stress σ_H was set at 1.12 MPa.

The injection pressure is controlled by a servo hydraulic pump with the maximum capacity of fluid injection pressure of 80 MPa. Fracturing fluid with a viscosity of 1 MPa·s was injected into the simulation wellbore during the tests. Meanwhile, red tracer was added into the fracturing fluid for better monitoring characteristics of hydraulic fractures during hydraulic fracturing. In addition, a constant flow rate of 10 ml/min was adopted.

2.2.3. Ultrasonic Equipment and Measuring Technique. The ultrasonic equipment used in this study consists of pulser/receiver portable ultrasonic tester device manufactured by

TABLE 1: Mixing proportions of samples with different sand sizes.

Series	Water	Cement	Clay	Mass (kg)				28-day tensile strength σ_t (MPa)	28-day fracture toughness $K_{IC}(\text{MPa}\cdot\text{m}^{0.5})$
				2–2.36 mm	0.355–0.425 mm	0.125–0.15 mm	0.063–0.075 mm		
M8	4	10	20	20				1.544	0.403
M40	4	10	20		20			1.805	0.487
M100	4	10	20			20		1.007	0.364
M200	4	10	20				20	0.961	0.227

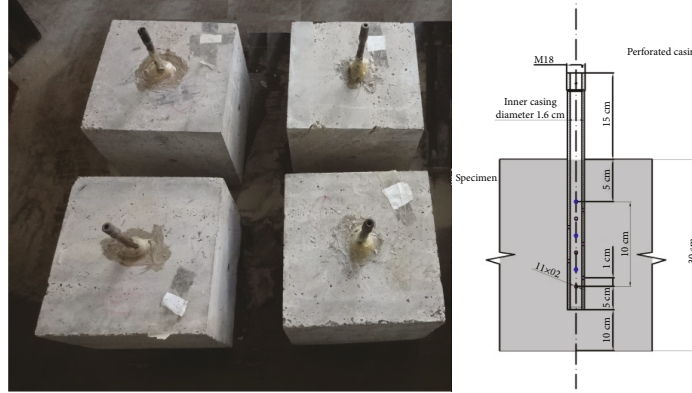


FIGURE 4: The prepared specimens and the sketch of perforated casing.

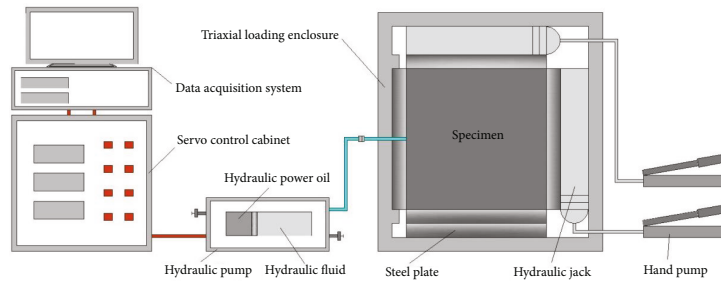


FIGURE 5: Schematic diagram showing the system used for the hydraulic fracturing experiments.

Koncrete Engineering Testing Technology Ltd. Measurement amplitudes were conducted at several cross sections of the concrete samples. The transducers were placed on the opposite side along the minimum horizontal principal stress and the maximum vertical principal stress, respectively. Measurements were repeated 27 times at different points at intervals of 0.03 m vertically and 0.05 m laterally. Figure 6 shows the testing arrangement of the transducers for ultrasonic testing.

The use of low frequencies in the range of 40–80 kHz for evaluating concrete is recommended [30]. In both disturbed and undisturbed conditions, the specimens under examination were ultrasonically evaluated using a 50 kHz frequency transducer as transmitter and receiver. The signals were transmitted into the specimen at the voltage level of 500 V. The transmitter and receiver were tightly bonded exactly at opposite concrete specimen surfaces, using a special viscoelastic silicone gel as couplant. The couplant provided excellent conductivity. Figure 7 shows the typical time domain

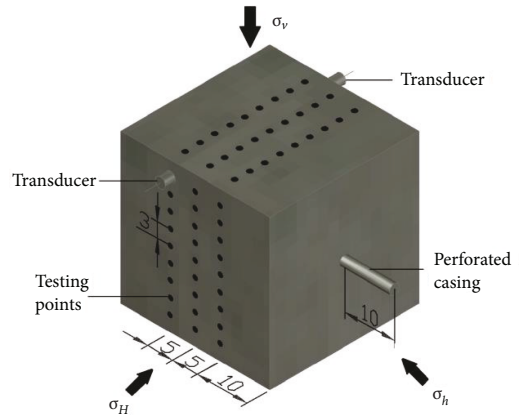


FIGURE 6: Test specimen and transducer location.

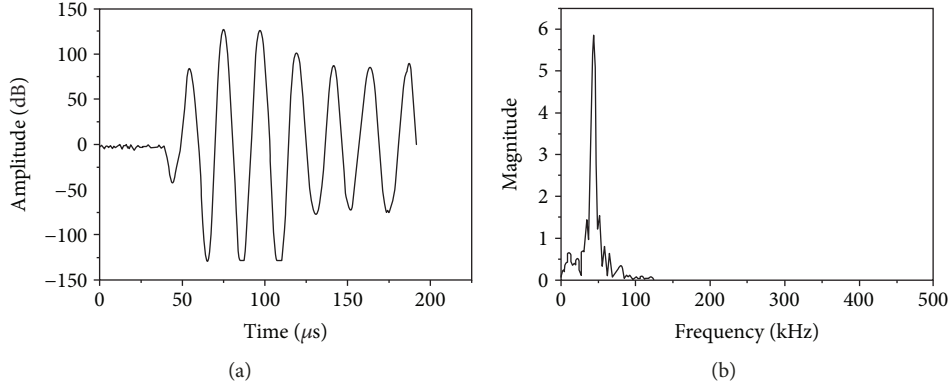


FIGURE 7: Typical time domain waveforms and frequency domain waveforms using 50 kHz transmitter.

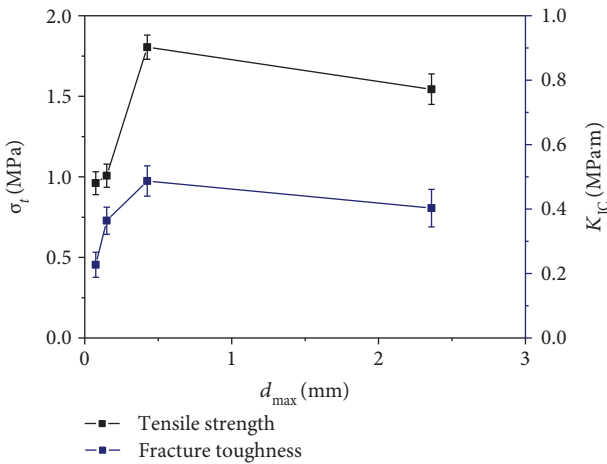


FIGURE 8: Variation of σ_t and K_{IC} of specimens with different maximum brittle mineral sizes.

and frequency domain waveforms received by the transducers, and the detected signals were analyzed and recorded in terms of various waveform parameters.

3. Results and Discussion

3.1. Fracture Toughness. Figure 8 shows the relationships among the tensile strength, fracture toughness (K_{IC}), and maximum brittle mineral size (d_{max}). It can be seen that both tensile strength and fracture toughness increase with increase in maximum brittle mineral size when the maximum brittle mineral size is smaller than 0.425 mm. However, when the brittle mineral size is larger than 0.425 mm, both tensile strength and fracture toughness decrease with increase in maximum brittle mineral size. The results show that, at a fixed value of total brittle mineral content, the larger average brittle mineral size is directly proportional to a larger size of the fracture area.

The highest values of σ_t and K_{IC} are achieved by a specimen with maximum brittle mineral size of 0.425 mm, probably because the size and strength of these brittle minerals enhance the development of tortuous fracture surfaces. A specimen with a maximum brittle mineral size of 2.36 mm presents even smaller values of σ_t and K_{IC} . These brittle

minerals develop very high interface bonds, and although there is some cracking, but it is not significant. Consequently, there is a reduction in σ_t and K_{IC} .

3.2. Fracture Pressure. Figure 9 shows the tested sample with different maximum brittle mineral sizes as well as the relationship of pump pressure and time during the hydraulic fracturing experiment on the samples with different brittle mineral sizes. Along the curve (Figure 10(a)), the segment OA depicted the idle stroke stage; in segment AB, the pump pressure increased rapidly and initial cracks began to expand and develop; in segment BC, the pump pressure increased steadily and cracks began to develop and propagate; at point C, the pump pressure reached maximum; in segment CD, cracks in the sample run through and the fracturing fluid rapidly permeated into the cracks leading to a sharp decline in pressure; in segment DE, the pump pressure was roughly stable; and in segment EF, the curve fluctuated quickly and then followed the existing trends of the pump pressure. The pump pressure curve of the other samples was identical with the sample with maximum brittle mineral size of 2.36 mm, except for the curve fluctuation of segment EF.

The fracture pressure is closely related to the fracture propagation in hydraulic fracturing process in the shale. There is an obvious correlation between the degree of fracture pressure and the brittle mineral size (Figure 11). The fracture pressure increased with the increase of brittle mineral size from 0.075 mm to 0.425 mm and then decreased when the brittle mineral size continued to increase from 0.425 mm to 2.36 mm. For shale, it is well known that the interfacial zone between matrix and brittle minerals is weaker than the brittle minerals [31, 32]. Cracks prefer to propagate along the interfacial zone. Therefore, when brittle mineral size increases, large brittle minerals debond and deflect cracks, resulting in provision of more energy needed for cracking and then higher values of fracture pressure. A specimen with a maximum brittle mineral size of 0.425 mm presents values of fracture pressure substantially higher than the other specimen (on the order of 10% -18%), probably due to a greater branching of cracks induced by sharp edges and surface texture of the brittle minerals. The effects of brittle minerals on bonding, deflecting, and bridging cracks decrease, which are most probably because the more original

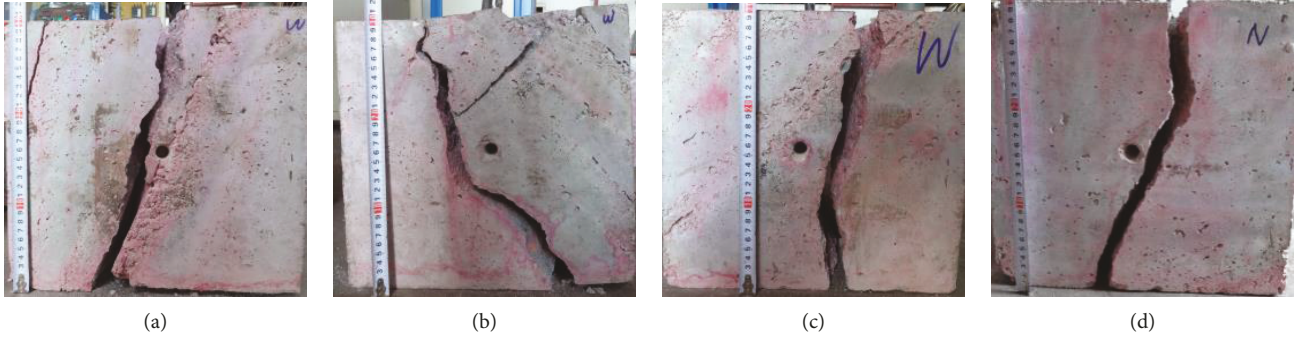


FIGURE 9: Random fracture distribution on the surface after hydraulic fracturing for different brittle mineral sizes. (a) 2.36 mm. (b) 0.425 mm. (c) 0.15 mm. (d) 0.075 mm.

fissures deteriorate in large brittle minerals [33, 34]. More cracks passing through brittle minerals were more pronounced in the specimens with larger maximum-size brittle minerals. Therefore, less energy is needed for cracking and resulting lower value of fracture pressure.

3.3. Attenuation. The examination of the amplitude of the signals at different stages of the specimens revealed the interesting features related to the brittle mineral size, because the amplitude of the electric input signal was held constant throughout the experimental series using the same transducers and changes in the amplitude can be attributed directly to the attenuative behavior of the samples. Generally, the most important mechanisms of attenuation in such complicated systems include intrinsic (absorption) and extrinsic (scattering) mechanisms such as absorption losses in each of the individual phases (fractures) and visco-inertial losses due to density discrepancies of the constituent materials [35–37]. In order to minimize the random effects, the measurements were all conducted by the same operator following the same procedure throughout the experimental series of this work. Therefore, different attenuation in measured signal of samples before and after hydraulic fracturing was attributed in the nature of material and induced fractures of the material itself.

The attenuation coefficient is determined by measuring the reduction in the amplitude of an ultrasonic wave which has traveled a known distance through a sample and is given by

$$\alpha = -\frac{20}{x} \log \left(\frac{A_x}{A_0} \right), \quad (1)$$

where A_0 is the initial amplitude of the wave and A_x is the amplitude after it has traveled a distance x . The output wave amplitude (A_x) is the absolute peak voltage of the received signal, while the amplitude of the pulse entering the specimen was measured separately on a face to face configuration of the transducers [38].

To quantify the difference between disturbed and undisturbed samples, the attenuation difference coefficient is proposed, which is given by

$$\beta = \alpha' - \alpha, \quad (2)$$

where α' is the attenuation of disturbed samples and α is the attenuation of undisturbed samples. The contour maps were created using the attenuation difference values by Kriging interpolation methods, as can be seen in Figure 12. The attenuation difference coefficient is directly proportional to the flexural fracture path. Comparison with specimens sharing the same parameters of total amount of brittle minerals and the correlation of attenuation difference with brittle mineral size are depicted clearly.

It is revealed that irrespective of the brittle mineral particle size of the specimens, the attenuation difference follows the same increasing trend from the center of casing to the periphery. However, the intensity of attenuation difference decreases with decrease in brittle mineral size except specimens with a brittle mineral size of 2.36 mm. This difference in attenuation can be attributed to the presence of different sizes of brittle minerals in specimens. In the near wellbore, the fracture usually follows the straight line. However, with the increase of brittle mineral size, the resistance effect of brittle minerals increases. When a fracture encounters a small particle, the resistance effect is relatively weak and the fracture can easily travel around the particle with no deflection. When a fracture encounters a larger particle, the resistance effect is relatively strong and the fracture must accumulate a sufficient amount of energy to overcome the resistance, then deflect or branch and stray considerably with more branches from straight lines. It indicates that cracks were extending more complicated from the center to the samples' periphery with larger brittle mineral particles. This is consistent with the conclusion stated above that the brittle mineral particle size strongly influences fracture extending.

3.4. Fracture Development under Electron Microscope. In order to study the crack propagation behavior of specimens with different brittle mineral sizes in-depth, fracture characteristics from hydraulic specimen's surface were examined in the scanning electron microscope.

Figure 13 shows different fracture paths for specimens with different maximum aggregate sizes under hydraulic fracturing tests with a stereo microscope. As can be seen in these figures, there are four obvious mechanisms of crack propagation in concrete which is the crack penetration through the aggregates Figure 13(a), crack deflection around

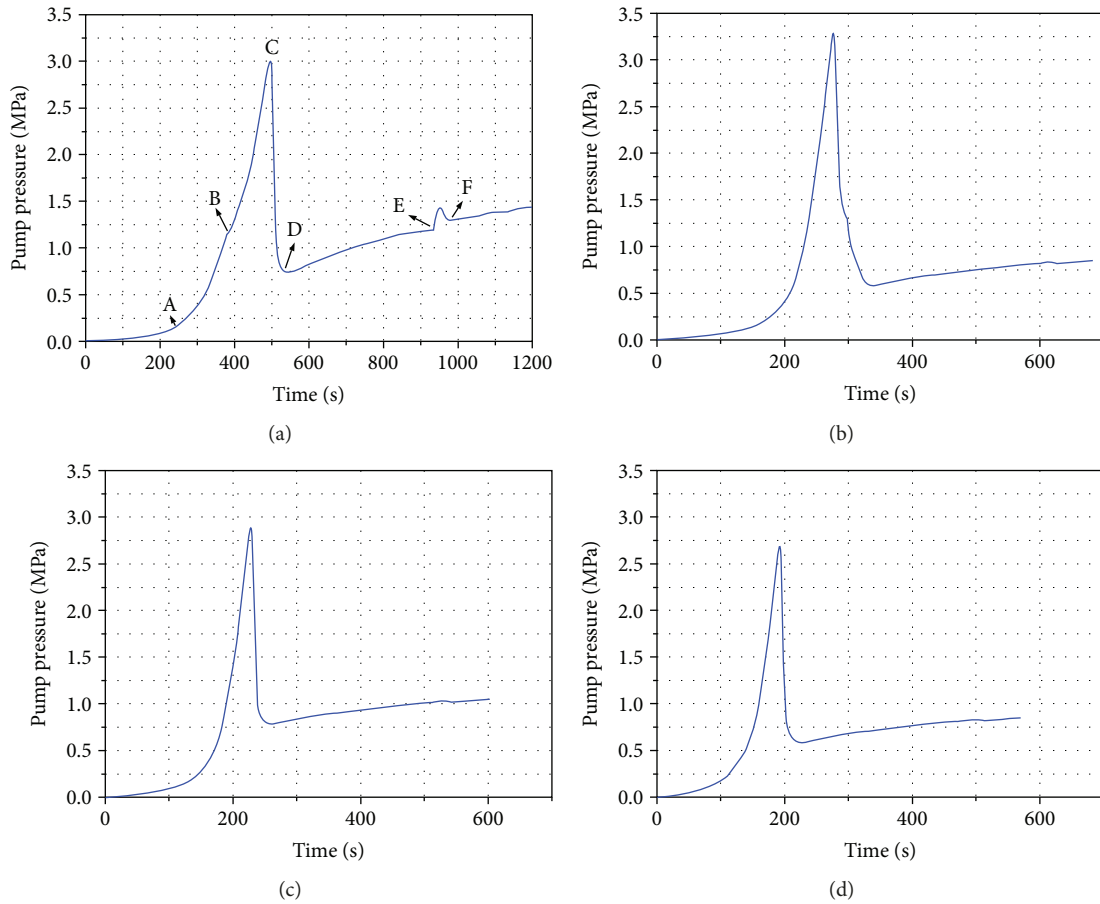


FIGURE 10: Relationship between hydraulic fracturing time and pumping pressure for different brittle mineral particle size (a) 2.36 mm. (b) 0.425 mm. (c) 0.15 mm. (d) 0.075 mm.

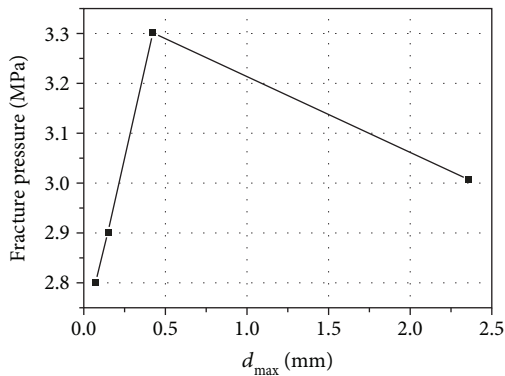


FIGURE 11: Relationship between maximum brittle mineral size and fracture pressure.

the aggregates Figure 13(b), crack passing through matrix only Figure 13(c), and crack termination at the aggregates Figure 13(d). The different crack extension behaviors of each specimen were counted, and the relationship between hydraulic fracture extension behavior and maximum aggregate size of each specimen was obviously noted (Figure 14). Observed fractures generally negotiate around aggregates when the maximum aggregate size is smaller than 0.425 mm.

However, for specimens with maximum aggregate sizes of 2.36 mm, hydraulic fracture paths were generally observed to penetrate through the aggregate. The deflections are the most common fracture patterns, especially the specimen with smaller brittle mineral size, regardless of whether the fracture strikes the particle or approaches at an offset from the particle. When the magnitude of the fracture-tip stress is sufficiently high, penetrations are likely to occur. Otherwise, penetrations can only occur within the large brittle mineral with fissures in it.

Figure 15 shows the mean deflection angle of sample's surfaces with different brittle mineral sizes measured by a photosensitive electron microscope. The crack path that deviates from the centerline of the specimen increases from 4.654° to 43.767° with an increase in the maximum aggregate size. Fracture deflection by particles can enhance the fracture growth resistance which reduces the energy release rate [39, 40]. When a fracture encounters a small brittle mineral, the fracture can easily travel around it with little or even no deflection angle due to the relatively weak resistance effect. With the increase in the brittle mineral size, the deflection angle increased. It reveals that the size of the brittle particles also affects the crack deflection during hydraulic fracturing. More tortuous cracks in samples may be found with larger brittle particles.

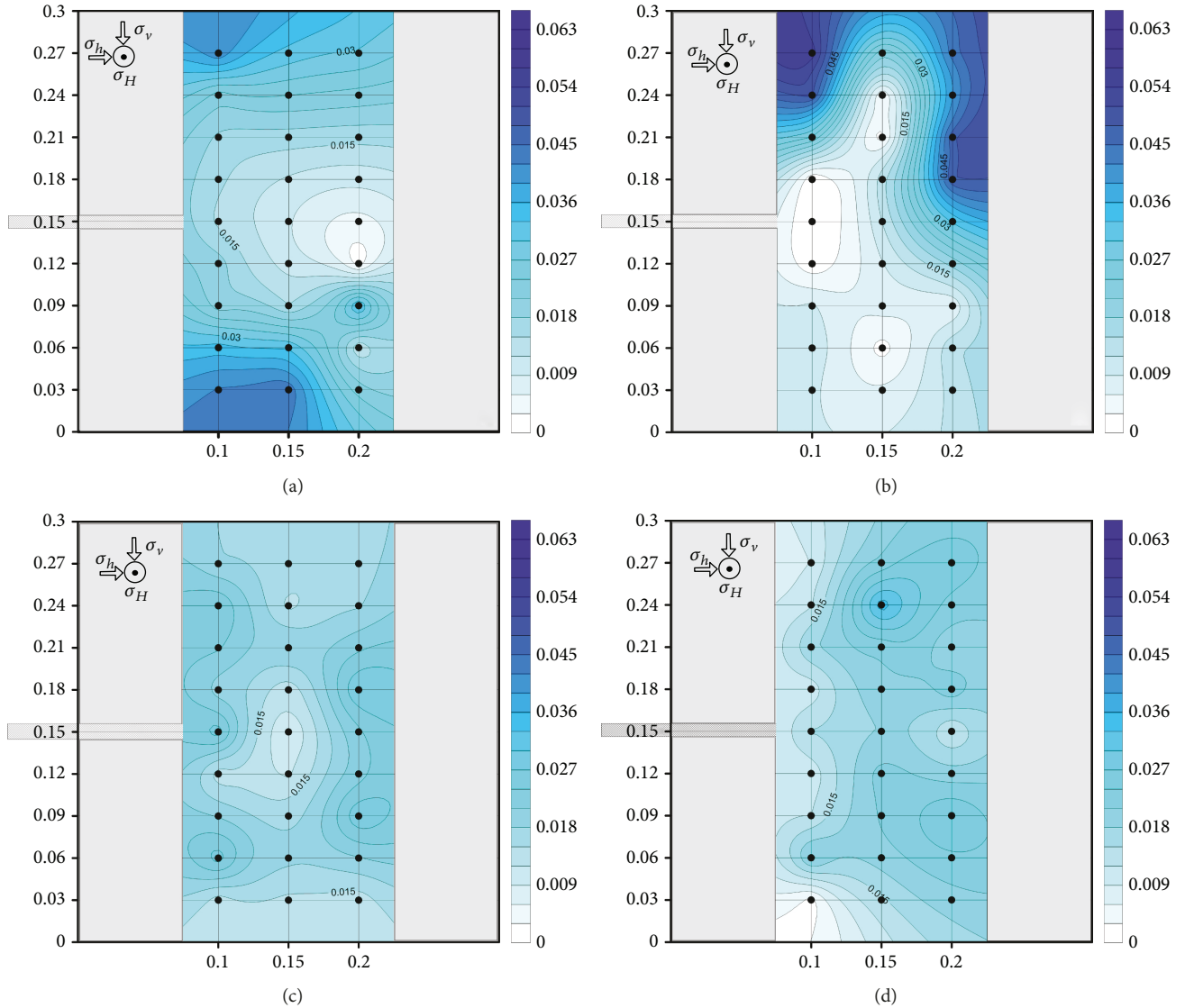


FIGURE 12: Maps of attenuation difference between disturbed and undisturbed samples with different brittle mineral particle sizes. (a) 2.36 mm. (b) 0.425 mm. (c) 0.15 mm. (d) 0.075 mm.

It is well known that cracks prefer to propagate along the weaker interfacial zone or pores in the matrix [41–44]. As the crack meets a brittle mineral particle, it is forced either to propagate through the tougher particle or deflect and travel around the particle-matrix interface. Since the interface toughness is usually lower than the matrix, the advancing crack is prone to deflect the brittle mineral, resulting in a tortuous cracking path. Tortuous cracking path generation increases with the increase in maximum size of brittle minerals. However, when brittle minerals are large enough to have some natural microfissuring in it, the fractures penetrate through the aggregate instead of deflection around the aggregate (Figure 16). This result is consistent with the hydraulic fracturing process deduced from numerical analysis techniques in hydraulic fracturing simulation conducted by some researchers (Chen et al., 2018; [45, 46]).

4. Numerical Simulation for Hydrofracturing Crack Initiation and Propagation

The previous laboratory experimental research shows that brittle mineral size is one of the most important factors influencing the hydraulic fracture propagation. To better understand the effects of brittle mineral size difference on the propagation behavior of hydrofracturing cracks and compare these against laboratory experimental results, the hydraulic fracturing simulations were performed based on a two-dimensional particle flow code.

4.1. Fluid-Mechanical Coupling in PFC^{2D}. The material is represented as an aggregate of numerous rigid circular particles in PFC^{2D} [47, 48], and Cundall's algorithms were adopted to simulate the fluid flow [49]. Figure 17 shows the basic mechanism of the fluid-mechanical coupling [50].

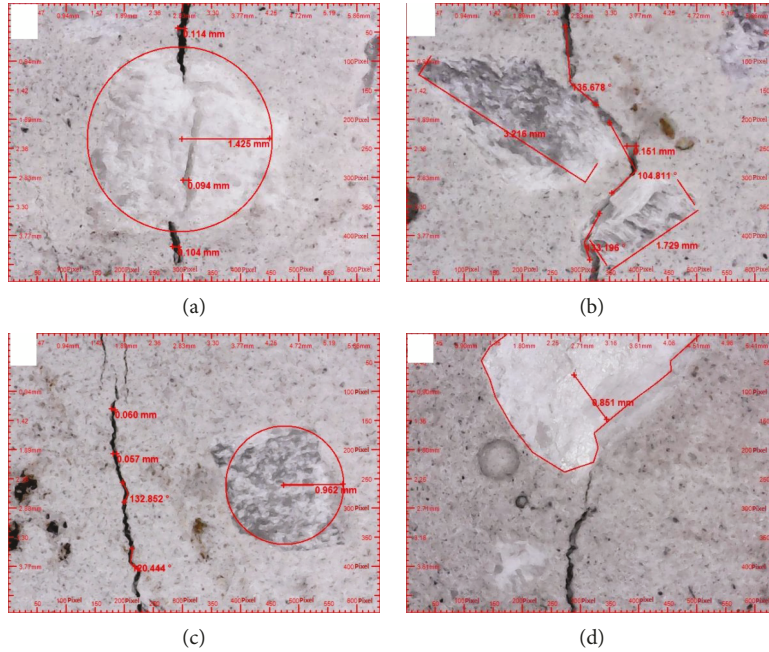


FIGURE 13: The fracture propagation behavior under hydraulic fracturing tests. (a) Crack penetration through the aggregate. (b) Crack deflection around the aggregate. (c) Crack passing through matrix only. (d) Crack termination at the aggregate.

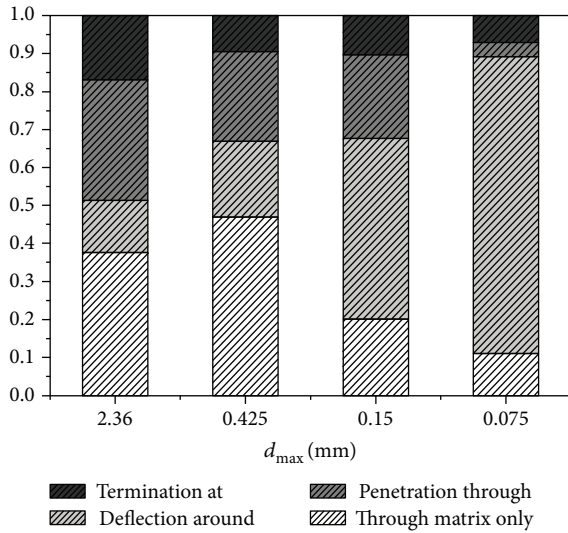


FIGURE 14: Relationship between hydraulic fracture extension behavior and maximum grain size.

The motion of the particles and the contact force between particles are calculated by Newton’s second law and the force-displacement law, respectively. The fluid flow is calculated by the cubic law [49]. For more details, refer to Potyondy and Cundall [48].

The particles around the reservoir move and deform due to the fluid pressure within each calculation step. So the domain volume and the hydraulic aperture of the flow channel change subsequently, and the flow and fluid pressure need to be updated. A new fluid pressure exerts on the particles after the fluid calculation step.

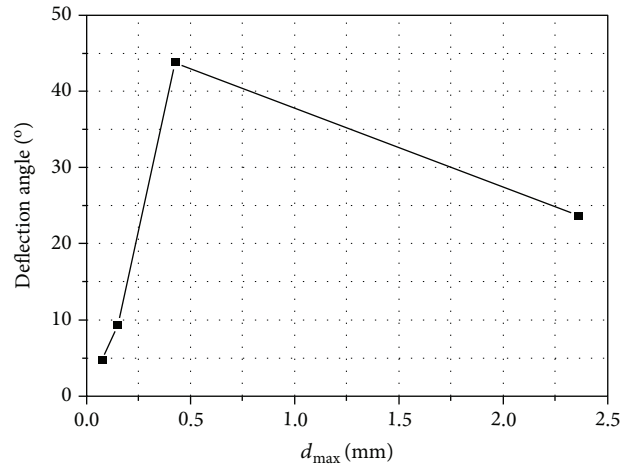


FIGURE 15: The mean deflection angle of specimen’s surface with different brittle mineral sizes.

4.2. Model Description and Parameters. In this study, the model is expressed by the assembly of particles bonded with each other. The size of the specimen used for hydraulic fracturing simulation is 300 mm in width and 300 mm in height. As shown in Figure 18, the model is surrounded by the four confining walls which are represented by green dotted particles. The motion of the walls can be controlled by a servo-adjustment method to apply a constant confining pressure in the x -direction (S_H) and y -direction (S_h). A borehole for fluid injection is created at the center of the model with the diameter of 16 mm. In order to make the borehole walls smoother and to avoid unnecessary stress concentration, the particles that have the half of the model mean particle

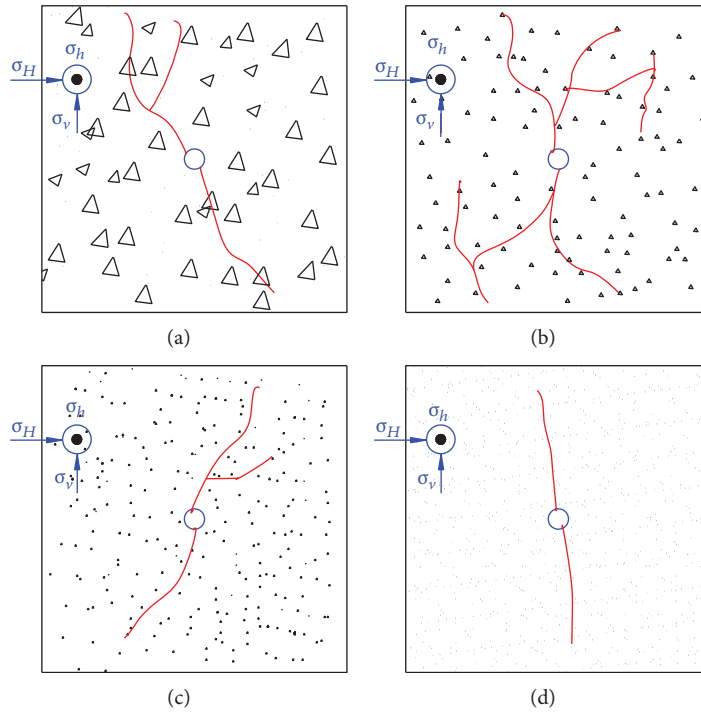


FIGURE 16: Fracture propagation sketch with different brittle mineral particle sizes. (a) 2.36 mm. (b) 0.425 mm. (c) 0.15 mm. (d) 0.075 mm.

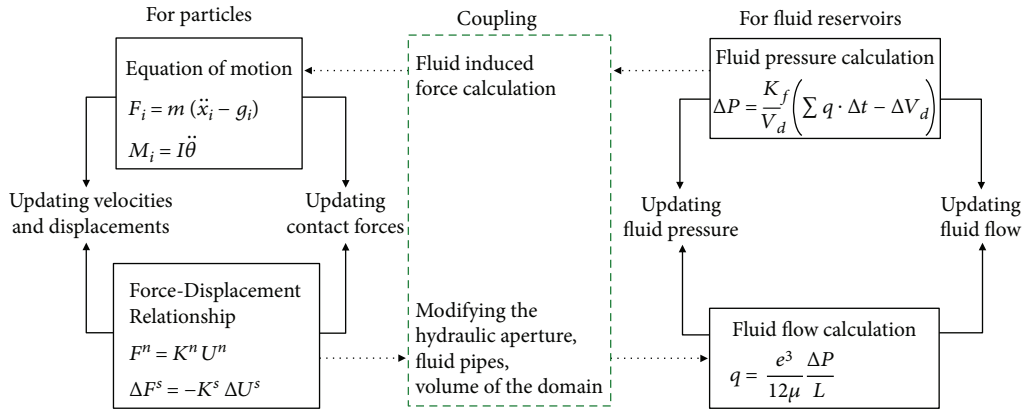


FIGURE 17: The basic mechanism of fluid-mechanical coupling (after[50]).

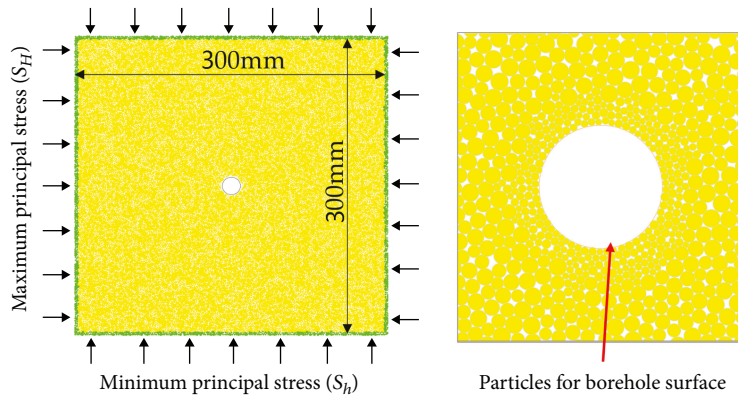


FIGURE 18: Numerical specimen model and particle packing method near the borehole.

TABLE 2: Physicomechanical parameters employed in the simulation.

Mold	Parameters	Notations	Values
Particle	Density (kg/m^3)	ρ	2680
	Young's modulus (GPa)	E	35
	Ratio of normal to shear stiffness	$\frac{k_n}{k_s}$	1.5
	Friction coefficient	f	0.4
Parallel bond	Tensile strength (MPa)	σ_c	60
	Ratio of normal to shear stiffness	$\frac{\bar{k}_n}{\bar{k}_s}$	1.5
	Shear strength (MPa)	τ_c	110
	Young's modulus (GPa)	E_c	35
	Radius multiplier	λ	1
Hydraulic properties	Moment contribution factor	β	1
	Bulk modulus of the fracturing fluid (GPa)	K_f	2
	Viscosity (Pa·s)	μ	1.0×10^{-3}
	Initial hydraulic aperture (m)	e_0	1.0×10^{-6}
	Permeability (m^2)	k	1.0×10^{-17}
	Velocity (m^3/s)	\mathbf{v}	1.5×10^{-4}

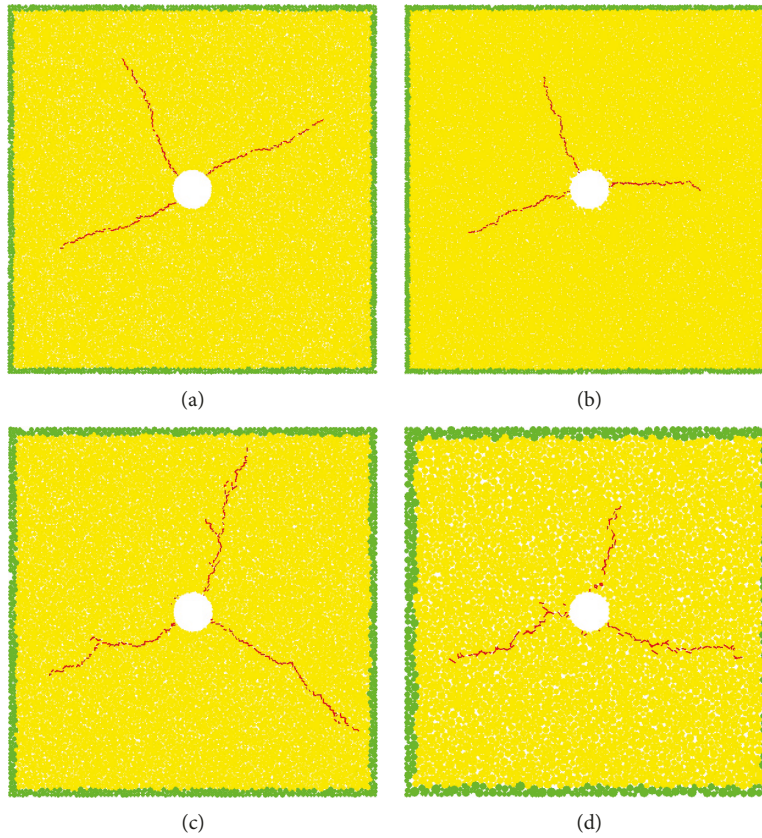


FIGURE 19: Numerically obtained fractured pattern of the specimens with different particle sizes. (a) Maximum particle diameter $d = 0.075$ mm. (b) Maximum particle diameter $d = 0.15$ mm. (c) Maximum particle diameter $d = 0.425$ mm. (d) Maximum particle diameter $d = 2.36$ mm.

radius are arranged in the circular form at the center of the model to form the inner wall of the borehole [50].

The microscopic mechanical parameters used in this simulation, which is mainly a trial-and-error procedure, were calibrated on the basis of the experimental results. In this study, macroscopic mechanical properties of shale in the Chang-7 (C7) member, Yanchang Formation in the south-eastern Ordos Basin, were used to calibrate the microscopic parameters including elastic modulus, peak strength, and Poisson's ratio. After a trial-and-error process, the elastic modulus, peak strength, and Poisson's ratio of the calibration model were determined to be 25 GPa, 103 MPa, and 0.24, respectively, which are in good agreement with the experimental results. The mesoscopic physical and mechanical parameters of the model and the fluid parameters used for hydraulic fracturing are shown in Table 2.

Four models are employed in this section. Each of these models has the same brittle mineral volume content (40%) but different brittle diameters (2.36, 0.425, 0.15, and 0.075 mm, respectively). In each model, all the particles are distributed randomly. All of the models are subject to the same confining stresses like laboratory experimental dose.

The numerical results are listed in Figure 19. The general trend of the numerical results is consistent with the laboratory tests except the result with brittle mineral size of 2.36 mm, which is probably because the property of brittle minerals used in experiment and simulation tests was different.

The overall fracturing patterns in the four models are consistent with the laboratory experiments results. The fracture generation profiles are characterized by numerous deflections, branchings, and terminations. The fracturing trajectory on the local scale is clearly dominated by the brittle minerals, especially the large brittle minerals. When large brittle minerals are encountered, the fracture is typically deflected and moving around them in most of the cases. However, in some cases, the fracture is terminated when it strikes the brittle minerals head-on and instead of penetrating through the brittle minerals. In some cases, the initial fracture trajectory does not intersect the brittle minerals; the fracture is nevertheless attracted by the particle as it approaches. We did not compare the numerical results with the experimental ones quantitatively because these were 2D simulations, and the shapes and distributions of the brittle minerals in the simulations are not completely consistent with those in the experiments.

5. Conclusions

- (1) Both tensile strength and fracture toughness increase with the increase in maximum brittle mineral size when the maximum brittle mineral size is smaller than 0.425 mm. It is observed that at a fixed value of total brittle mineral content, the larger average brittle mineral size corresponds to a larger size of the fracture area
- (2) Ultrasonic technique can provide useful information regarding crack propagation inside the materials.

Ultrasonic tests in this study show that increasing maximum brittle mineral size can increase the degree of attenuation difference between the disturbed and undisturbed specimens. This is due to the reason that brittle minerals can deflect propagating cracks in the matrix and create bigger fracture process zone

- (3) Observed mesofracture morphology reveals that tortuous and complicated cracking path generation increases with the increase in maximum size of brittle mineral
- (4) When brittle minerals are large enough to have some natural microfissuring in it, such as maximum brittle mineral size larger than 0.425 mm, the tensile strength and fracture toughness decrease
- (5) The influences of the brittle mineral size on the fracturing pattern are numerically investigated. The fracturing path is clearly dominated by the brittle mineral, especially larger particles, which is consistent with the laboratory results

Data Availability

The data used to support the findings of this study are available from the corresponding author upon request.

Conflicts of Interest

All authors do not have any conflict of interest.

Acknowledgments

This work was financially supported by the Strategic Priority Research Program of the Chinese Academy of Sciences (Grant no. XDB10030104), the National Natural Science Foundation of China (41330643), and the Chinese Academy of Sciences President's International Fellowship Initiative (Grant no. 2018PC0009).

References

- [1] J. Dai, C. Zou, D. Dong et al., "Geochemical characteristics of marine and terrestrial shale gas in China," *Marine and Petroleum Geology*, vol. 76, pp. 444–463, 2016.
- [2] D. Dong, Y. Wang, X. Li et al., "Breakthrough and prospect of shale gas exploration and development in China," *Natural Gas Industry B*, vol. 3, no. 1, pp. 12–26, 2016.
- [3] T. Guo, S. Zhang, Z. Qu, T. Zhou, Y. Xiao, and J. Gao, "Experimental study of hydraulic fracturing for shale by stimulated reservoir volume," *Fuel*, vol. 128, pp. 373–380, 2014.
- [4] F. Hao, H. Zou, and Y. Lu, "Mechanisms of shale gas storage: implications for shale gas exploration in China," *AAPG Bulletin*, vol. 97, no. 8, pp. 1325–1346, 2013.
- [5] P. Liu, Y. Feng, L. Zhao, N. Li, and Z. Luo, "Technical status and challenges of shale gas development in Sichuan Basin, China," *Petroleum*, vol. 1, no. 1, pp. 1–7, 2015.
- [6] C. Zou, D. Dong, Y. Wang et al., "Shale gas in China: characteristics, challenges and prospects (I)," *Petroleum Exploration and Development*, vol. 42, no. 6, pp. 753–767, 2015.

- [7] C. Zou, D. Dong, Y. Wang et al., "Shale gas in China: characteristics, challenges and prospects (II)," *Petroleum Exploration and Development*, vol. 43, no. 2, pp. 182–196, 2016.
- [8] B. Yuan and D. A. Wood, "Production analysis and performance forecasting for natural gas reservoirs: theory and practice (2011–2015)," *Journal of Natural Gas Science and Engineering*, vol. 26, pp. 1433–1438, 2015.
- [9] B. Yuan, D. A. Wood, and W. Yu, "Virtual special issue: stimulation and hydraulic fracturing technology in natural gas reservoirs: theory and case studies (2012–2015)," *Journal of Natural Gas Science and Engineering*, vol. 26, pp. 1508–1509, 2015.
- [10] B. Yuan, D. Zheng, R. G. Moghanloo, and K. Wang, "A novel integrated workflow for evaluation, optimization, and production prediction in shale plays," *International Journal of Coal Geology*, vol. 180, pp. 18–28, 2017.
- [11] T. Guo, S. Zhang, H. Ge, X. Wang, X. Lei, and B. Xiao, "A new method for evaluation of fracture network formation capacity of rock," *Fuel*, vol. 140, pp. 778–787, 2015.
- [12] Z. Liu and Z. Sun, "New brittleness indexes and their application in shale/clay gas reservoir prediction," *Petroleum Exploration and Development*, vol. 42, no. 1, pp. 129–137, 2015.
- [13] C. Zou, D. Dong, S. Wang et al., "Geological characteristics and resource potential of shale gas in China," *Petroleum Exploration and Development*, vol. 37, no. 6, pp. 641–653, 2010.
- [14] C. R. Clarkson, N. Solano, R. M. Bustin et al., "Pore structure characterization of North American shale gas reservoirs using USANS/SANS, gas adsorption, and mercury intrusion," *Fuel*, vol. 103, pp. 606–616, 2013.
- [15] W. Ding, C. Li, C. Li et al., "Fracture Development in Shale and Its Relationship to Gas Accumulation," *Geoscience Frontiers*, vol. 3, no. 1, pp. 97–105, 2012.
- [16] X. Li, Z. Lu, D. Dong, and K. Cheng, "Geologic controls on accumulation of shale gas in North America," *Natural Gas Industry*, vol. 29, no. 5, pp. 27–32, 2009.
- [17] K. A. Bowker, "Barnett shale gas production, Fort Worth Basin: issues and discussion," *AAPG Bulletin*, vol. 91, no. 4, pp. 523–533, 2007.
- [18] K. Piszcz, J. Luczak, and J. Hupka, "Mobility of shale drill cuttings constituents," *Physicochemical Problems of Mineral Processing*, vol. 50, no. 2, pp. 795–810, 2014.
- [19] H. Baioumy, Y. Ulfa, M. Nawawi, E. Padmanabhan, and M. N. A. Anuar, "Mineralogy and geochemistry of Palaeozoic black shales from Peninsular Malaysia: implications for their origin and maturation," *International Journal of Coal Geology*, vol. 165, pp. 90–105, 2016.
- [20] X. Li, J. Zhang, Y. Wang et al., "Accumulation conditions of Lower Paleozoic shale gas from the southern Sichuan Basin, China," *Journal of Natural Gas Geoscience*, vol. 1, no. 2, pp. 101–108, 2016.
- [21] Y. X. Yu, *Pore-Structure and Petrophysical Properties of Silt Laminae in Lacustrine Gas Shale: Example from the Yanchang Group, Ordos Basin*, China University of Petroleum (East China), 2013.
- [22] D. M. Jarvie, R. J. Hill, T. E. Ruble, and R. M. Pollastro, "Unconventional shale-gas systems: the Mississippian Barnett Shale of north-central Texas as one model for thermogenic shale-gas assessment," *AAPG Bulletin*, vol. 91, no. 4, pp. 475–499, 2007.
- [23] F. P. Wang and J. F. W. Gale, "Screening criteria for shale-gas systems," *Gulf Coast Association of Geological Societies Transactions*, vol. 59, pp. 779–793, 2009.
- [24] R. Gholami, V. Rasouli, M. Sarmadivaleh, V. Minaeian, and N. Fakhari, "Brittleness of gas shale reservoirs: a case study from the north Perth basin, Australia," *Journal of Natural Gas Science and Engineering*, vol. 33, pp. 1244–1259, 2016.
- [25] E. Rybacki, T. Meier, and G. Dresen, "What controls the mechanical properties of shale rocks? – part II: brittleness," *Journal of Petroleum Science and Engineering*, vol. 144, pp. 39–58, 2016.
- [26] X. Tang, J. Zhang, X. Wang et al., "Shale characteristics in the southeastern Ordos Basin, China: implications for hydrocarbon accumulation conditions and the potential of continental shales," *International Journal of Coal Geology*, vol. 128–129, pp. 32–46, 2014.
- [27] M. Enderlin, H. Alsleben, and J. Beyer, "Predicting fracability in shale reservoirs," AAPG Annual Convention and Exhibition, Houston, Texas, USA, 2011.
- [28] T. Ishida, S. Sasaki, I. Matsunaga, Q. Chen, and Y. Mizuta, "Effect of grain size in granitic rocks on hydraulic fracturing mechanism Trends in Rock Mechanics," in *Trends in Rock Mechanics. Proceedings of Sessions of Geo-Denver 2000*, pp. 128–139, ASCE Geotechnical Special Publication, Denver, Colorado, 2000.
- [29] T. Ishida, "Acoustic emission monitoring of hydraulic fracturing in laboratory and field," *Construction and Building Materials*, vol. 15, no. 5–6, pp. 283–295, 2001.
- [30] P. A. Gaydecki, F. M. Burdekin, W. Damaj, and D. G. John, "The propagation and attenuation of medium-frequency ultrasonic waves in concrete: a signal analytical approach," *Measurement Science and Technology*, vol. 3, no. 1, pp. 126–134, 1992.
- [31] U. Akesson, J. Hansson, and J. Stigh, "Characterisation of microcracks in the Bohus granite, western Sweden, caused by uniaxial cyclic loading," *Engineering Geology*, vol. 72, no. 1–2, pp. 131–142, 2004.
- [32] I. Rigopoulos, B. Tsikouras, P. Pomonis, and K. Hatzipanagiotou, "Petrographic investigation of microcrack initiation in mafic ophiolitic rocks under uniaxial compression," *Rock Mechanics and Rock Engineering*, vol. 46, no. 5, pp. 1061–1072, 2013.
- [33] J. S. Chester, S. C. Lenz, F. M. Chester, and R. A. Lang, "Mechanisms of compaction of quartz sand at diagenetic conditions," *Earth and Planetary Science Letters*, vol. 220, no. 3–4, pp. 435–451, 2004.
- [34] R. H. Brzesowsky, S. J. T. Hangx, N. Brantut, and C. J. Spiers, "Compaction creep of sands due to time-dependent grain failure: effects of chemical environment, applied stress, and grain size," *Journal of Geophysical Research: Solid Earth*, vol. 119, no. 10, pp. 7521–7541, 2014.
- [35] A. A. Shah and Y. Ribakov, "Non-destructive evaluation of concrete in damaged and undamaged states," *Materials and Design*, vol. 30, no. 9, pp. 3504–3511, 2009.
- [36] A. A. Shah, Y. Ribakov, and S. Hirose, "Nondestructive evaluation of damaged concrete using nonlinear ultrasonics," *Materials and Design*, vol. 30, no. 3, pp. 775–782, 2009.
- [37] K. Warnemuende and H.-C. Wu, "Actively modulated acoustic nondestructive evaluation of concrete," *Cement and Concrete Research*, vol. 34, no. 4, pp. 563–570, 2004.
- [38] T. P. Philippidis and D. G. Aggelis, "Experimental study of wave dispersion and attenuation in concrete," *Ultrasonics*, vol. 43, no. 7, pp. 584–595, 2005.

- [39] P. Grassl and M. Jirásek, "Meso-scale approach to modelling the fracture process zone of concrete subjected to uniaxial tension," *International Journal of Solids and Structures*, vol. 47, no. 7-8, pp. 957-968, 2010.
- [40] L. Li, Q. Meng, S. Wang, G. Li, and C. Tang, "A numerical investigation of the hydraulic fracturing behaviour of conglomerate in glutenite formation," *Acta Geotechnica*, vol. 8, no. 6, pp. 597-618, 2013.
- [41] T. Akçaoglu, M. Tokyay, and T. Çelik, "Effect of coarse aggregate size and matrix quality on ITZ and failure behavior of concrete under uniaxial compression," *Cement and Concrete Composites*, vol. 26, no. 6, pp. 633-638, 2004.
- [42] M. H. A. Beygi, M. T. Kazemi, I. M. Nikbin, J. Vaseghi Amiri, S. Rabbanifar, and E. Rahmani, "The influence of coarse aggregate size and volume on the fracture behavior and brittleness of self-compacting concrete," *Cement and Concrete Research*, vol. 66, pp. 75-90, 2014.
- [43] G. Giaccio and R. Zerbino, "Failure mechanism of concrete: combined effects of coarse aggregates and strength level," *Advanced Cement Based Materials*, vol. 7, no. 2, pp. 41-48, 1998.
- [44] M. C. Torrijos, G. Giaccio, and R. Zerbino, "Mechanical and transport properties of 10 years old concretes prepared with different coarse aggregates," *Construction and Building Materials*, vol. 44, pp. 706-715, 2013.
- [45] P. Liu, Y. Ju, P. G. Ranjith, Z. Zheng, and J. Chen, "Experimental investigation of the effects of heterogeneity and geostress difference on the 3D growth and distribution of hydrofracturing cracks in unconventional reservoir rocks," *Journal of Natural Gas Science and Engineering*, vol. 35, pp. 541-554, 2016.
- [46] H. Shimizu, S. Murata, and T. Ishida, "The distinct element analysis for hydraulic fracturing in hard rock considering fluid viscosity and particle size distribution," *International Journal of Rock Mechanics and Mining Sciences*, vol. 48, no. 5, pp. 712-727, 2011.
- [47] P. A. Cundall, "Computer simulations of dense sphere assemblies," in *Studies in Applied Mechanics*, M. Satake and J. T. Jenkins, Eds., pp. 113-123, 1988.
- [48] D. O. Potyondy and P. A. Cundall, "A bonded-particle model for rock," *International Journal of Rock Mechanics and Mining Sciences*, vol. 41, no. 8, pp. 1329-1364, 2004.
- [49] P. A. Cundall, *Fluid Formulation for PFC2D*, Itasca Consulting Group, Minneapolis, MN, USA, 2000.
- [50] J. Zhou, L. Zhang, A. Braun, and Z. Han, "Numerical modeling and investigation of fluid-driven fracture propagation in reservoirs based on a modified fluid-mechanically coupled model in two-dimensional particle flow code," *Energies*, vol. 9, no. 9, p. 699, 2016.



Hindawi

Submit your manuscripts at
www.hindawi.com

